Nanoscale Advances

PAPER

View Article Online
View Journal | View Issue

Cite this: *Nanoscale Adv.*, 2025, 7, 7964

Silicon nanowire based angle robust ultrasensitive hyperbolic metamaterial biosensor

Badhan Golder, † Zahidul Salman,† Rony Das and Arif Ahammad *

We design an angle-robust hyperbolic metamaterial-based biosensor structure using n-doped silicon nanowires. We examine the hyperbolic properties of the structure using effective medium theory (EMT) and analyze the resonance shift of our proposed biosensor structure, by employing the finite-difference time domain (FDTD) method, and theoretically verify the result with the transfer matrix method (TMM). Our proposed sensor structure exhibited a perfect reflectance shift for impedance matching and extreme anisotropic properties at the NIR wavelength ($\lambda > 2.2$ μm). We analytically demonstrate the electric field confinement between nanowires by employing the resonance condition, which is enhanced by the total internal reflection (TIR) phase shift. We demonstrate that the angle-insensitive characteristic is inherited by the extreme anisotropic hyperbolic dispersion relation and analyze the effect of structural parameters on the bulk sensitivity using the dispersion relation to optimize the sensor parameters. We explore the sensor performance for detecting the dengue virus and demonstrate that our proposed sensor can detect a single dengue NS1 protein with an outstanding sensitivity of a resonant wavelength shift of 14 nm per NS1 protein and mass sensitivity of 0.192 nm kDa^{-1}. We analyze the ideal limit of detection (LOD) of the NS1 protein solution from the diffusion equation and elucidate that the geometry of the n-Si NW exhibits an unprecedented LOD of 0.691 pM. Our proposed biosensor can be effectively employed for the ultra-sensitive, highly precise label-free detection of various viruses and bacteria at the nanoscale limit.

Received 25th July 2025
Accepted 1st October 2025

DOI: 10.1039/d5na00714c

rsc.li/nanoscale-advances

1 Introduction

Plasmonic materials are key to designing robust optical device structures, such as sensors,[1] absorbers,[2] waveguides,[3] polarizers,[4] and antennas.[5] Some sensors used the optical properties of plasmonic materials in order to achieve label-free biosensing[6] and chemical identification.[7] Free electrons oscillate at the metal–dielectric interface at the resonance wavelength in plasmonic nanostructures, known as surface plasmon resonance (SPR). Moreover, surface plasmon polaritons (SPPs) are electromagnetic (EM) waves that propagate at the interface of metals and dielectric materials, and localized surface plasmon (LSP) resonance is the confinement in metallic nanoparticles. Due to the phenomenon of momentum matching and field confinement, the rate of molecule detection using SPP-based sensors is exceptionally high, achieving a sensitivity of nearly 3000 nm per RIU (ref. 8) or more. However, this kind of sensor encounters challenges in detecting nanoscale samples and exhibits angle sensitivity, which is a significant issue given the modern nanoscale size of the analyte.[9] Although LSP-based sensors can detect smaller molecules[1] due to enhanced field confinement compared to SPPs, their sensitivity is lower than that of SPPs. Researchers are now interested in metamaterial-based plasmonic sensors, which address the limitations of conventional plasmonic sensors in nanoscale studies.[10,11] However, these types of sensors face challenges in detecting smaller quantities of lower molecular weight molecules (<500 Da) due to their reduced polarizability, and the figure of merit (FOM) of this sensor is relatively low. However, these sensors are very useful for detecting harmful viruses such as dengue,[12] malaria,[13] *etc.* The dengue virus, a member of the Flaviviridae family, contains nonstructural protein 1 (NS1), which is found in all flaviviruses and plays a crucial role in viral life cycle processes such as replication and immune evasion. The concentration of the NS1 protein in host blood increases rapidly with viral replication.[14] Although electrochemical sensors, which are different from plasmonic sensors, have achieved high glucose sensitivity,[15] HMM biosensors offer label-free, real-time detection with greater selectivity.

Recently, researchers have introduced extreme anisotropic metamaterials known as hyperbolic metamaterials (HMMs), which addressed the limitations of conventional metamaterial-based plasmonic sensors. Unlike other types of metamaterials, HMMs have the unique property of exhibiting hyperbolic dispersion, as the directions of their perpendicular and parallel polarization are opposite to one another.[16] This exceptional

---

Department of Electrical and Electronic Engineering, Shahjalal University of Science and Technology, Sylhet-3114, Bangladesh. E-mail: arif-eee@sust.edu

† These authors contributed equally to this work.

property applies to various fields, including hyperlenses,[17] enhanced spontaneous emission,[18] *etc.* Moreover, HMMs are highly suitable for sensor applications and field confinement due to the excitation of high-*k* modes.[19] The design of HMMs, which are based on an array of layers or nanowires, along with the strong interactions between them, enhances sensitivity to variations in the refractive index (RI). Hong-Zhuo *et al.* introduced a multilayer structure of Ag and TiN_xO_y designed for RI sensing, achieving a sensitivity of 2475.20 nm per RIU.[20] Moreover, Sreekanth *et al.* proposed an extremely sensitive multilayered HMM structure for detecting molecules for improved medical applications.[21] Unlike sensitivity, fabricating multilayers is more complex than fabricating nanowires. Moreover, nanowire-based HMMs are more effective in detecting nanoscale molecules and providing geometrical effects on the limit of detection (LOD). Vasilantonakis *et al.* proposed a gold (Au) nanowire-based ultrasensitive HMM sensor for chemical and biomedical purposes.[22] Moreover, Ruoqin *et al.* proposed and fabricated a gold (Au) nanowire-based HMM sensor in the field of biosensing to detect the binding of streptavidin (a protein).[23] These proposed structures are based on noble metals such as Au and Ag. However, they exhibit high optical losses, leading to degraded device performance.[24] Sarker *et al.* proposed a TiN nanowire-based HMM sensor for detecting *E. coli*, showing that nanowire HMM sensors can be made from other plasmonic materials.[25] Researchers have found a new plasmonic material made from other semiconductor like Si,[26] which overcomes the limitations of noble metals. Additionally, n-doped silicon (Si) is a more convenient alternative to noble metals exhibiting negative real permittivity. Moreover, the carrier concentration of n-doped Si can be controlled by meticulous doping and optimized for both the real and imaginary components of permittivity.[27] As a result, researchers have utilized the properties of n-doped Si in plasmonic sensors as an alternative to noble metals.[27–29] Moreover, the effect of n-doped Si nanowire-based HMM sensor structures on device performance has not yet been studied. A significant drawback of earlier HMM sensors is their inability to provide consistent responses with varying incident angles. However, angle robustness is indispensable for an HMM sensor to reduce the noise for accurate detection of a minimal change in molecular properties. Even a small variation of the resonant frequency over different incident angles significantly affects the LOD of the HMM sensor.

In this study, we proposed a highly sensitive angle-robust biosensor structure employing strong light confinement within the HMM nanostructure, based on an n-doped silicon (n-Si) nanowire to leverage hyperbolic properties. We analyzed the proposed nanowire-based HMM biosensor structure employing effective medium theory (EMT), the finite difference time domain (FDTD), and the transfer matrix method (TMM). We obtained the hyperbolic region for the structure using the Maxwell–Garnett equation. Moreover, we analyzed the confinement of light within our nanostructure based on the resonance phase condition. Furthermore, we investigated the angle independence of our structure using both the FDTD and TMM. After that, we optimized the geometrical parameters based on reflection spectra using the numerical sweep method. Additionally, we investigated the mode frequency shift using EMT equations. We studied the sensor performance for dengue application by injecting the NS1 protein. We examined the mass sensitivity and diffusion time of the molecules for binding on the n-Si NW surface at different molar concentrations of NS1 solution. Additionally, for level-free real-time monitoring, we analyzed the LOD based on a fixed, reliable time to bind a single molecule. Finally, we performed a comprehensive comparison of the performance parameters of our proposed HMM sensor with those in previously reported studies.

2 Methodology

We designed an n-doped Si (n-Si)-based HMM structure and analyzed its sensor performance in the NIR region. We conducted the numerical analysis using the FDTD method and analytical calculation using the TMM and EMT method. Fig. 1(a) shows the 3D view of our proposed HMM structure, containing a n-Si nanowire (NW) and base. Fig. 1(b) illustrates the simulation setup of a unit cell for the FDTD method. Our proposed structure was periodic in the *x*- and *y*-directions. Moreover, we used perfectly matched layer (PML) boundary conditions in the *z*-direction. We employed both transverse magnetic (TM) and transverse electric (TE) polarized light sources by adjusting the polarization angle ($\phi = 0°$ and $90°$, respectively). The numerical analysis was conducted in the wavelength range of 1500 to 5000 nm. Moreover, we analyzed the reflection spectra by changing the incident angle value θ in our structure. We employed power monitors to calculate the reflection, transmission, and absorption of our proposed sensor structure using

$$T(\lambda) = \frac{P_t(\lambda)}{P_i(\lambda)}, \quad (1)$$

$$R(\lambda) = \frac{P_r(\lambda)}{P_i(\lambda)}, \text{ and} \quad (2)$$

$$A(\lambda) = 1 - T(\lambda) - R(\lambda) \quad (3)$$

Here, $T(\lambda)$, $R(\lambda)$, and $A(\lambda)$ represent the transmission, reflection, and absorption of our proposed sensor structure varying with λ, respectively. $P_t(\lambda)$, $P_r(\lambda)$, and $P_i(\lambda)$ represent the transmitted, reflected, and incident powers, respectively. We set a fixed temperature of 300 K to conduct the numerical analysis. We optimized the unit cell's geometrical parameters by applying a parametric sweep. We calculated the radius (r) of our proposed biosensor structure based on the fill factor (FF), as illustrated in Fig. 1(c), determined using

$$\text{FF} = \frac{\pi r^2}{P^2}. \quad (4)$$

Here, P denotes periodicity, which was 80 nm, and the FF was 70% in our study. The height of the n-Si NW (h_n) was 80 nm, and the height of the base (h_b) was 200 nm, as illustrated in Fig. 1(d). Fig. S1 in the SI provides a suggested fabrication technique

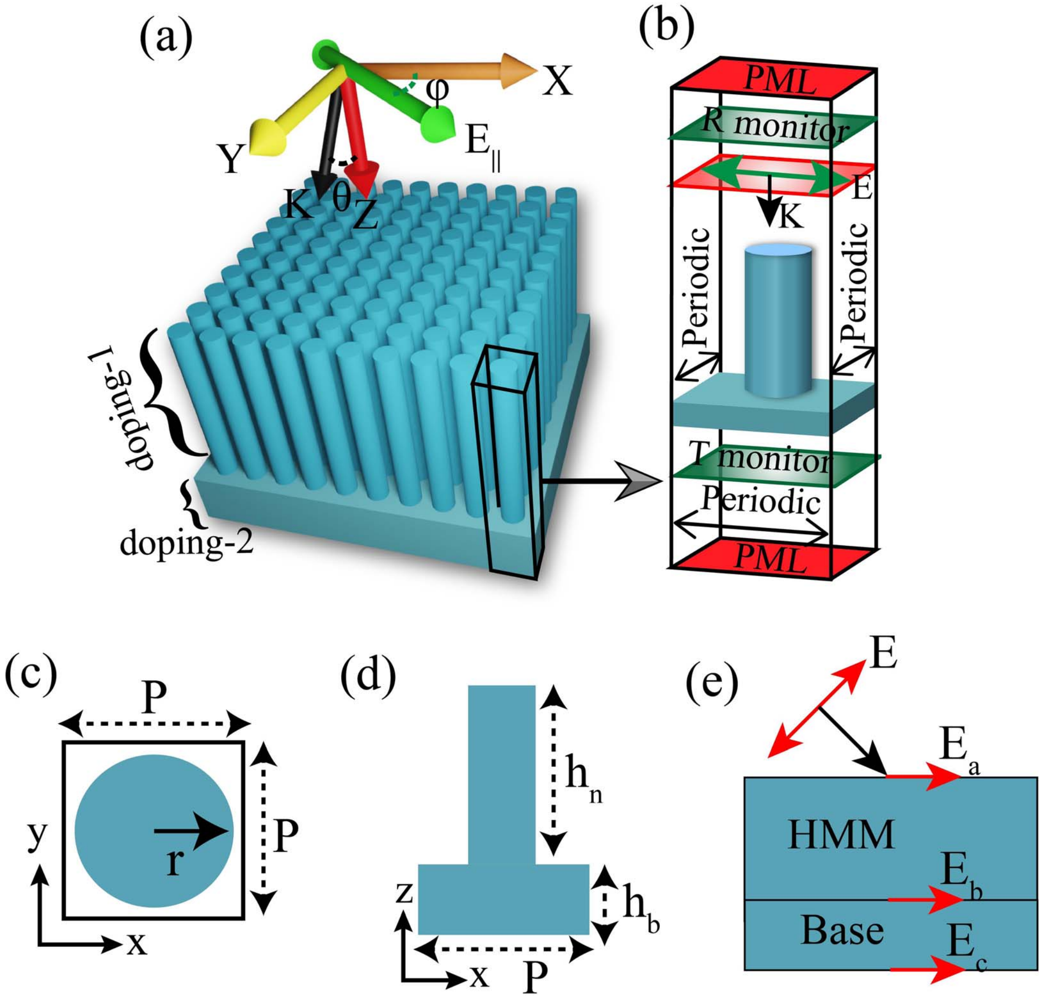

Fig. 1 (a) The 3D illustration of the proposed n-Si based hyperbolic metamaterial biosensor structure with different doping concentrations of the nanowire (doping-1) and base (doping-2), where θ and ϕ are the incident and polarization angles of a plane wave with the propagation direction (k). (b) The FDTD simulation setup of a unit cell with boundary conditions, a plane wave, and monitors. (c) The xy- and (d) xz-views, where P, r, h_n, and h_b are the periodicity, radius, height of the nanowire, and height of the base of the biosensor structure. (e) The tangential electric field (E_a, E_b, and E_c) at the interfaces of the equivalent thin film TMM of the biosensor structure.

employing electron beam lithography (EBL) and electroplating to fabricate n-Si NW-based HMM structures. We determined the permittivity (ε) of n-Si using the Drude–Lorentz equation:[17]

$$\varepsilon(\omega) = \varepsilon_\infty - \frac{{\omega_p}^2}{\omega^2 + j\gamma\omega}, \text{ and} \tag{5}$$

$$\omega_p = \sqrt{\frac{Ne^2}{\varepsilon_0 m^*}}. \tag{6}$$

Here, ω_p, γ and ε_∞ are the plasma frequency, damping coefficient, and static permittivity of bulk n-Si. ε_0, e, and m^* are vacuum permittivity, charge, and effective mass of an electron & N is the doping concentration of n-Si. We adopted 1×10^{21} cm^{-3} and 7×10^{20} cm^{-3} as the NW doping concentration (doping-1) and the base doping concentration (doping-2) of n-Si, respectively. The relative permittivity of the different doping concentrations of n-Si is illustrated in Fig. S2 in the SI. The impact of doping concentration of the NW and base on reflection spectra is illustrated in Fig. S3 in the SI. We introduced freshwater employing a background RI of 1.333. We calculated the NS1 protein's RI which is 1.5, as discussed in Section 3 in the SI. We analyzed the hyperbolic properties and mode frequency shift of our proposed biosensor structure using the EMT and dispersion relation, which is detailed further in later sections. Furthermore, we analyzed the reflectance of our n-Si NW HMM structure using the TMM. The equivalent optical layer is shown in Fig. 1(e). The TMM model for our proposed biosensor structure is given as[30,31]

$$\begin{bmatrix} \dfrac{E_a}{E_c} \\ \dfrac{H_a}{E_c} \end{bmatrix} = \begin{bmatrix} \cos\delta_{\mathrm{HMM}} & \dfrac{i\sin\delta_{\mathrm{HMM}}}{\eta_{\mathrm{HMM}}} \\ i\eta_{\mathrm{HMM}}\sin\delta_{\mathrm{HMM}} & \cos\delta_{\mathrm{HMM}} \end{bmatrix} \times \begin{bmatrix} \cos\delta_{\mathrm{base}} & \dfrac{i\sin\delta_{\mathrm{base}}}{\eta_{\mathrm{base}}} \\ i\eta_{\mathrm{base}}\sin\delta_{\mathrm{base}} & \cos\delta_{\mathrm{base}} \end{bmatrix} \begin{bmatrix} 1 \\ \eta_o \end{bmatrix} \tag{7}$$

Here, E_a, H_a, E_c, and H_c are the tangential electric and magnetic fields at the boundary interfaces a and c (top and bottom). η_{HMM}, η_{Au}, δ_{HMM}, and δ_{Au} are the optical admittance and propagation phase within the HMM and Au layer, which are defined as

$$\delta_{\text{HMM}} = \sqrt{k_{\text{o}}\left(n_{\text{HMM}}{}^2 - n_{\text{o}} \sin \theta^2 - k_{\text{HMM}}{}^2 - 2in_{\text{HMM}} \times k_{\text{HMM}}\right)}h_{\text{n}}, \tag{8}$$

$$\eta_{\text{HMM}} = \frac{\delta_{\text{HMM}}}{k_{\text{o}}h_{\text{n}}}\eta_{\text{o}}, \tag{9}$$

$$\delta_{\text{base}} = \sqrt{k_{\text{o}}\left(n_{\text{base}}{}^2 - n_{\text{o}} \sin \theta^2 - k_{\text{base}}{}^2 - 2in_{\text{base}} \times k_{\text{base}}\right)}h_{\text{b}}, \text{ and} \tag{10}$$

$$\eta_{\text{base}} = \frac{\delta_{\text{base}}}{k_{\text{o}}h_{\text{b}}}\eta_{\text{o}}. \tag{11}$$

Here, n_{o}, n_{HMM}, n_{base}, k_{o}, k_{HMM}, and k_{base} are the corresponding refractive index and wavenumber of vacuum, the HMM and the Au layer. η_{o} is the optical admittance of vacuum. The admittance η measured using the incident wave from the top of the HMM layer was obtained using

$$\eta = \frac{\dfrac{H_a}{E_c}}{\dfrac{E_a}{E_c}} = \frac{H_a}{E_a}. \tag{12}$$

The reflection R and transmission T, utilizing the TMM, of our proposed biosensor structure are obtained from the Fresnel equation by equalizing the Poynting vector normal to the interface, as determined using

$$R = \left(\frac{\dfrac{\eta_{\text{o}}}{\cos\theta} - \eta}{\dfrac{\eta_{\text{o}}}{\cos\theta} + \eta}\right)\left(\frac{\dfrac{\eta_{\text{o}}}{\cos\theta} - \eta}{\dfrac{\eta_{\text{o}}}{\cos\theta} + \eta}\right)^*, \text{ and} \tag{13}$$

$$T = \frac{4\eta_{\text{o}}\text{Re}(\eta)}{\left(\eta_{\text{o}}\dfrac{E_{\text{a}}}{E_{\text{c}}} + \dfrac{H_{\text{a}}}{E_{\text{c}}}\right)\left(\eta_{\text{o}}\dfrac{E_{\text{a}}}{E_{\text{c}}} + \dfrac{H_{\text{a}}}{E_{\text{c}}}\right)^*}. \tag{14}$$

Additionally, we analyzed the point detection capability with the NS1 protein of our proposed HMM biosensor structure by following these steps. Firstly, we analyzed the effect of surface coverage by gradually covering the NW with NS1 solution from bottom to top. Secondly, we examined the effect of the binding position of the NS1 protein, modeled as a circular disk with a height of 8 nm, at various points of the NW. Finally, the binding effect of a single NS1 protein volume of ~90 nm^3 along the upper surface of the n-Si NW was investigated. Moreover, we calculated the equivalent homogeneous effective permittivity of the heterogeneous mixture of NS1 protein and water using the Maxwell–Garnett equation[32] to determine the LOD conventionally.

$$\varepsilon_{\text{eff}} = \frac{(1 + 2X)\varepsilon_{\text{d}}\varepsilon_{\text{w}} + 2\varepsilon_{\text{w}}{}^2(1 - X)}{(2 + X)\varepsilon_{\text{w}} + (1 - X)\varepsilon_{\text{d}}}. \tag{15}$$

Here, ε_{d} and ε_{w} represent the permittivities of the dispersive phase (NS1 protein) and continuous phase (water), respectively. X denotes the molar fraction of the dispersive phase. After that, we analyzed the geometrical impact of NS1 solution on the LOD by solving the diffusion equation, followed by[33]

$$\frac{\partial\rho}{\partial t} = D\nabla^2\rho, \tag{16}$$

$$J_{\text{t}} = D\nabla\rho. \tag{17}$$

We considered an ideal binding surface. Therefore, once a protein molecule binds to the functionalized NW surface, it does not desorb. This assumption limits the binding coefficient $k_{\text{f}} \to \infty$, and the biosensing process is treated as a diffusion-limited problem. Liu *et al.* justified highly adsorbing functionalized nanowires.[34] To mimic this molecular binding event, a Dirichlet boundary condition was imposed on the NW surface, allowing the molecules to sink into the NW. Therefore, the number of NS1 protein molecules bound to the NW surface is obtained using

$$\frac{\partial N}{\partial t} = k_{\text{f}}(N_0 - N)s = \int_{\text{surface}} j_{\text{t}} \times \text{d}A. \tag{18}$$

Here, ρ denotes the analyte concentration, N_0 indicates the total initial number of molecules, N signifies the number of captured molecules, j_{t} represents the molecular flux, D denotes the diffusion coefficient, and s indicates the binding site probability factor of the HMM biosensor structure.

3 Results and discussion

3.1 EM properties of the HMM

We measured the EM properties of the proposed HMM structure using EMT and obtained the permittivity tensor. The structure exhibited symmetry along the z-axis and periodicity in the transverse plane (x, y). The anisotropic behavior of our proposed structure came from the inhomogeneity and the polarization-direction dependence of the permittivity. We obtained permittivity along the principal axes using EMT, as expressed using[32]

$$\varepsilon_{xx} = \varepsilon_{yy} = \varepsilon_{\parallel} = \frac{(1 + \text{FF})\varepsilon_{\text{m}}\varepsilon_{\text{h}} + \varepsilon_{\text{h}}{}^2(1 - \text{FF})}{(1 + \text{FF})\varepsilon_{\text{h}} + (1 - \text{FF})\varepsilon_{\text{m}}}, \tag{19}$$

$$\varepsilon_{zz} = \varepsilon_{\perp} = \text{FF}\varepsilon_{\text{m}} + (1 - \text{FF})\varepsilon_{\text{h}} \tag{20}$$

Here, ε_{xx}, ε_{yy}, and ε_{zz} are the electric permittivity in the transverse direction (x and y plane) and perpendicular direction (z axis). ε_m, and ε_h are the permittivity of n-doped Si and the dielectric analyte, respectively. Because the permittivity properties of our proposed structure aligned with the coordinate axes, the permittivity tensor only had diagonal components, and the principal axes are in the x-, y- and z-directions. We conducted the frequency-dependent dispersion of permittivity tensor components $\varepsilon_{\parallel}$, and $\varepsilon_{\perp}$ from eqn (19) and (20). Moreover, the permittivity tensor $[\varepsilon]$ can be formed as[35]

$$[\varepsilon] = \begin{bmatrix} \varepsilon_{\parallel} & 0 & 0 \\ 0 & \varepsilon_{\parallel} & 0 \\ 0 & 0 & \varepsilon_{\perp} \end{bmatrix}, \tag{21}$$

The dispersion relation of the EM wave propagating into the structure can be obtained using Maxwell's curl equations:

$$\mathbf{k} \times (\mathbf{k} \times \mathbf{E}) = -\omega^2 \mu [\varepsilon] \mathbf{E}, \text{ and} \tag{22}$$

$$\begin{bmatrix} 0 & -k_z & 0 \\ k_z & 0 & -k_x \\ 0 & k_x & 0 \end{bmatrix}^2 \mathbf{E} = -\omega^2 \mu \begin{bmatrix} \varepsilon_{\parallel} & 0 & 0 \\ 0 & \varepsilon_{\parallel} & 0 \\ 0 & 0 & \varepsilon_{\perp} \end{bmatrix} \mathbf{E}. \tag{23}$$

We extracted the dispersion relation of the extraordinary wave by solving the eigenvalue equation:

$$\frac{{k_x}^2}{\varepsilon_{\perp}} + \frac{{k_y}^2}{\varepsilon_{\perp}} + \frac{{k_z}^2}{\varepsilon_{\parallel}} = {k_0}^2. \tag{24}$$

The transverse and perpendicular permittivity components $\varepsilon_{\parallel}$, and $\varepsilon_{\perp}$ of our structure are illustrated in Fig. 2(a). Hyperbolic dispersion can be categorized into two forms, one with $\varepsilon_{\parallel} > 0$, $\varepsilon_{\perp} < 0$, known as the type 1 HMM. In contrast, $\varepsilon_{\parallel} < 0$, $\varepsilon_{\perp} > 0$ corresponds to the type 2 HMM. Our proposed structure inherited the type 1 HMM characteristic for $\lambda > 2.2$ μm. Fig. 2(b) illustrates the dispersion relation plotted for an incident wave of $k_0 = \frac{2\pi}{4.5} \mu\text{m}^{-1}$.. The dispersive surface indicates the unique state of the wavevector of the refracted wave inside the NW HMM. Due to the extreme anisotropic nature of the NW HMM, the photonic density of states (PDOS) of our proposed structure was infinite compared to the finite photonic states of conventional isotropic and anisotropic materials. In contrast, for extensive wave vectors $k \sim 2\pi/P$, where P is the periodicity of the NW, the Maxwell–Garnett effective permittivity approximation failed. In this case, our structure no longer behaved as a homogeneous anisotropic medium, thereby limiting the available photonic states. However, the available photonic states were surprisingly larger than those in conventional anisotropic materials. This enhanced PDOS can confine light on a sub-wavelength scale and strengthen the interaction with the surrounding sensing materials. We obtained an increasing dispersive behavior of the relative permittivity with an increasing FF, as depicted in Fig. 2(c). Moreover, the increase in the FF shifted the hyperbolic region toward longer wavelengths. The effective $\varepsilon_{\perp}$ of our proposed structure exhibited the most negative behavior when the FF reached 70%, leading to extreme anisotropic behavior that enhanced the resonant effect and impedance matching. As a result, we achieved a perfect reflection dip at $\lambda = 2999$ nm, as illustrated in Fig. 2(d).

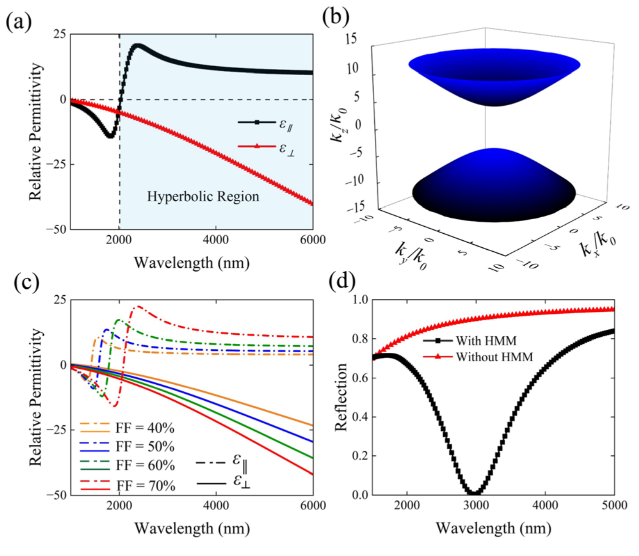

Fig. 2 (a) Illustration of the relative permittivity of our proposed n-Si nanowire HMM biosensor structure using EMT. The shaded portion represents the hyperbolic dispersion at $\lambda \geq 2000$ nm. (b) Illustration of the hyperbolic dispersion surface in photonic states, plotted with respect to the photon wavevector at a constant frequency of our proposed HMM biosensor structure. (c) Illustration of the effective permittivity components $\varepsilon_{\parallel}$ and $\varepsilon_{\perp}$ of n-Si nanowires over varying FFs. (d) Numerically calculated reflectance spectra for the proposed HMM biosensor structure with and without the HMM.

3.2 Confinement of light into the nanowire structure

We obtained similar reflection spectra for our proposed structure using the FDTD and TMM, as illustrated in Fig. 3(a). Moreover, the reflection dip (2999 nm) was accurate for both methods. The enhancement of the reflection dip was due to the resonance facilitated by the plasmonic mode. Furthermore, we demonstrated the confinement of light within our proposed structure by analyzing the electric field intensity at the transverse (x, y) and longitudinal (y, z) planes under a linearly polarized TM plane wave, as shown in Fig. 3(b). The geometrical distribution of the electric field intensity depends on the polarization direction of the plane wave source. The electric field was confined to the polarization direction, and the plasmons were only excited by the normal component of the electric field at the interface of the NW in our proposed structure. Consequently, the plasmons were not excited in the direction perpendicular to the electric field polarization. The plasmonic mode propagated along the longitudinal direction of the NW and decayed into the transverse plane. Hence, we found that light confinement was achieved at the NW interface, and the bulk plasmons were not excited, as illustrated in Fig. 3(c) and (d).

The propagating modes were reflected back and forth at the bottom and top interfaces of the NW, as shown in the inset of Fig. 3(e). The reflected waves were superimposed on each other, creating an interference and resonant effect inside the NW. The enhanced permittivity of the n-Si NW helped confine light within our proposed structure at the resonant wavelength. We achieved the resonance condition when the overall phase shift within our structure was equal to $n\pi$, where 'n' is the integer value 0, 1, 2… We calculated the total phase shift (ϕ_{total}) as follows:[36,37]

$$\phi_{\text{total}} = \phi_{\text{pro}} + \phi_{\text{NW-air}} + \phi_{\text{NW-base}}. \tag{25}$$

$$\lambda_n = \frac{2dk_z}{n\pi + \phi} \tag{26}$$

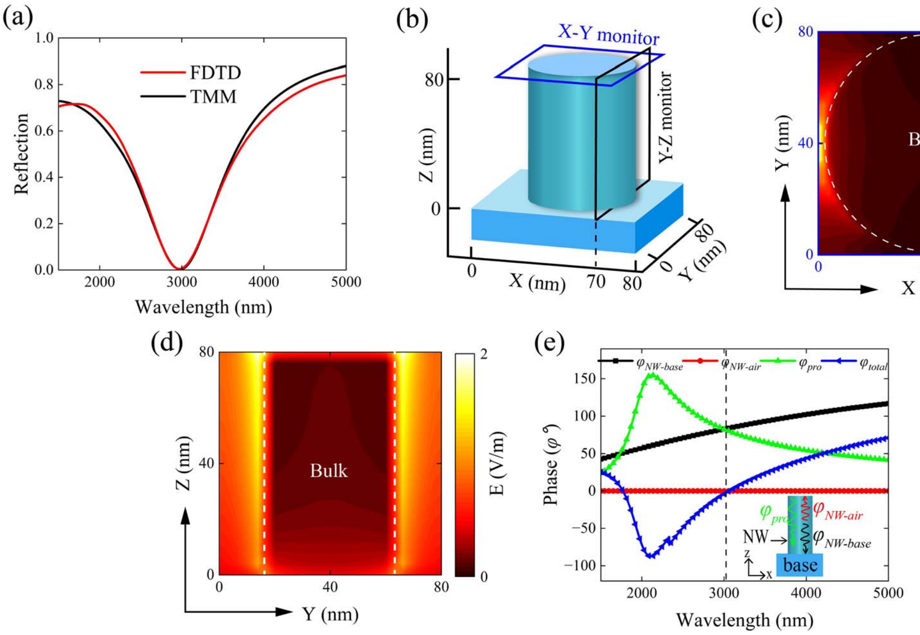

Fig. 3 (a) Numerically and analytically calculated reflection spectra using the FDTD and TMM. (b) The position of the electric field monitor in the X–Y and Y–Z directions of the biosensor structure. Visualization of the electric field ($|E|$) is shown in (c) X–Y and (d) X–Z views for the n-Si biosensor structure at $\lambda = 2999$ nm. The dotted line represents the bulk n-Si region. (e) The propagation phase shift ϕ_{pro} and the reflection phase shift at the n-Si NW and air interface $\phi_{\text{NW-air}}$ and n-Si NW and base interface $\phi_{\text{NW-base}}$ result in an overall phase shift ϕ_{total} experienced by a roundtrip of a photon in the n-Si NW.

Here, ϕ_{pro}, $\phi_{\text{NW-air}}$, and $\phi_{\text{NW-base}}$ are the propagation phase and non-trivial phase shifts at the top and bottom interfaces of the NW and also n, λ_n, ϕ, k_z, and d are the mode number, wavelength, TIR reflection, normal component of the wave vector at resonant wavelength, and the thickness of the NW, respectively. We studied the phase variables ϕ_{pro}, $\phi_{\text{NW-air}}$, and $\phi_{\text{NW-base}}$ by employing the TMM, as discussed in Section 5 in the SI. Fig. 3(e) illustrates the phase variables, indicating that the total phase shift ϕ_{total} at the resonant wavelength (2999 nm) almost satisfied the resonant condition of the 0th order resonance ($\phi_{\text{total}} = 0$), as described by eqn (26) for $n = 0$. This facilitated light confinement into the NW region, much smaller than the resonant wavelength itself, and enhanced the sensitivity of our proposed structure up to the nanoscale limit. Moreover, Yue *et al.* experimentally designed a highly sensitive plasmonic nanoridge HMM facilitated by a field confined between the nanoridge.[38] As the wavelength increased, the overall phase shift ϕ_{total} also increased, yet it remained smaller than 180°. Consequently, the resonance condition for higher-order modes to achieve the $n\pi$ phase shift to maintain constructive interference within the n-Si NW was not satisfied. As a result, only a single mode existed in our structure. This leads to enhanced detection accuracy, improved mode coupling, higher signal-to-noise ratio (SNR), and better spectral purity.

3.3 Impact of the incident angle

The angular dependence of the resonant wavelength in our proposed structure came from changes in the normal component of the incident wave vector. There was no tangential wave vector at the interface for normally incident light. Thus, the resonance wavelength is defined in eqn (26) and the normal component of the wave vector is defined by[32]

$$k_z^{\,2} = \varepsilon_{\parallel} k_o^{\,2} + \frac{\varepsilon_{\parallel} k_x^{\,2}}{\varepsilon_{\perp}}. \tag{27}$$

Unlike normal incidence, the resonant condition was affected by the angle of incidence as it introduces a tangential wave vector k_x, as shown in Fig. 4(a). The variation in k_x altered k_z, and consequently, the resonant wavelength λ_{n} was also affected by the angle of incidence. However, our proposed structure exhibited an extremely anisotropic hyperbolic dispersion relation. Concurrently, we found that the k_z at different angles of incidence remained unaffected for our structure. The robustness of k_z over k_x makes our structure completely insensitive to different incident angles of the TE plane wave. We investigated an unchanged behavior of the resonant wavelength for the TE wave at various incident angles using both the FDTD and TMM, as depicted in Fig. 4(b) and (d), respectively. Wu *et al.* experimentally designed an Ag nanoridge angle insensitive plasmonic hyperbolic tunable filter that confined light, facilitated by light funnelling.[39] In contrast, we observed a left shift in the resonant wavelength after an incident angle of 45° for the TM wave, using the FDTD and TMM, as shown in Fig. 4(c) and (e), respectively. This was due to the angle-dependent intrinsic admittance under TM waves.[30] The effect of angle-dependent reflection spectra can be mitigated using a coupled optical fiber with a numerical aperture (NA) lower than a 45° incident angle.[40] Moreover, we studied the

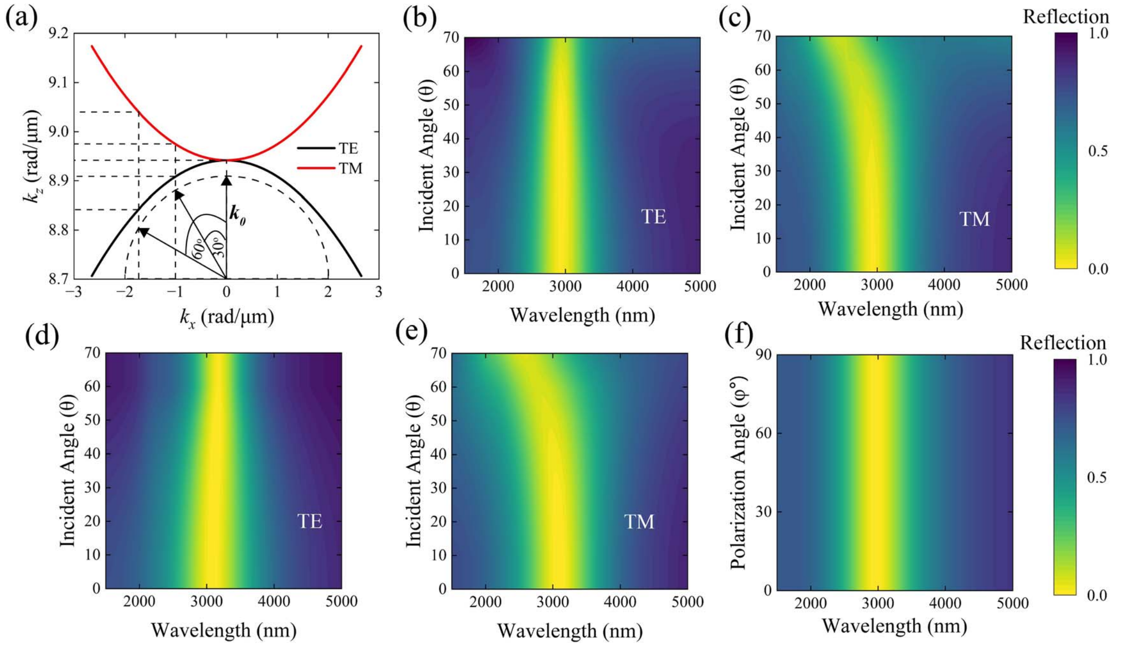

Fig. 4 (a) Illustration of incident light wave vector (k_0) at different incident angles θ in TE and TM modes and the corresponding tangential component (k_x) resulting in a longitudinal wave vector (k_z). The dotted half-circle represents the incident angle of light, while the arrow of particular k_0 connects corresponding k_x and k_z with the dotted line. Reflection spectra at varying incident angles (θ) for TE and TM modes, respectively, using (b and c) the FDTD method and (d and e) the TMM, respectively. (f) Reflection spectra at various polarization angles ϕ under TE and TM polarized light showing no shift in reflection for the symmetry of our proposed HMM structure.

resonant wavelength for different polarization angles under normal incidence, as shown in Fig. 4(f). Our structure was symmetrical to the x- and *y*-directions, so it was completely polarization-independent.

3.4 Impact of geometrical parameters

We optimized the geometrical parameters (h_n, h_b, and FF) based on the reflection spectra of our proposed sensor structure. We found that the reflection spectra were highly sensitive to h_n, as depicted in Fig. 5(a). We achieved stronger light confinement when h_n was set to 80 nm. The reflection of our structure increased as h_n increased or decreased. Thus, we determined the optimized value of the n-Si NW (h_n) to be 80 nm. Moreover, we studied the impact of h_b in our sensor structure, as illustrated in Fig. 5(b). We constantly observed a perfect reflection dip while varying the h_b. However, the FWHM increased when h_b was below 200 nm. The reflection spectra appeared quite similar after 200 nm. Thus, we adopted $h_b = 200$ nm for our study. Furthermore, we analyzed the effect of the FF by changing the NW radius (r) in our proposed sensor structure, as depicted in Fig. 5(c). We observed high reflection as the FF decreased, and the impedance matching was enhanced. Thus, we selected FF = 70% for our study. However, when we increased the FF above 70%, the NW began to overlap. Additionally, we studied the optimization and the impact of geometrical parameters analytically using the admittance diagram, as discussed in Fig. S4 in the SI.

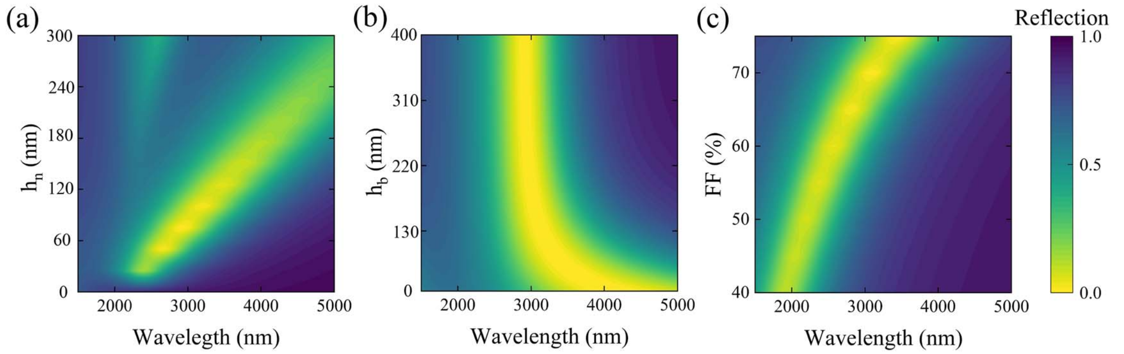

Fig. 5 Illustration of optimization of the geometrical parameters (a) h_n, (b) h_b and (c) FF on the reflection spectra for our proposed biosensor structure.

3.5 Dependence of mode frequency shift on the analyte R.I.

We investigated the mode frequency shift resulting from variations in the analyte's permittivity directly for the hyperbolic dispersion of our structure. The sensitivity of the mode frequency is obtained using[22]

$$\frac{\partial\omega_\mathrm{q}}{\partial\varepsilon_\mathrm{h,r}} = \frac{{C_0}^2}{2\omega_\mathrm{q}}\left[\left(\frac{k_x}{\varepsilon_\perp}\right)^2\frac{\partial\varepsilon_\perp}{\partial\varepsilon_\mathrm{h}} + \left(\frac{q\pi}{h_\mathrm{p}\varepsilon_\parallel}\right)^2\frac{\partial\varepsilon_\mathrm{d}}{\partial\varepsilon_\mathrm{h}}\right], \text{ and} \tag{28}$$

$$-i\frac{\partial\omega_\mathrm{q}}{\partial\varepsilon_\mathrm{h,i}} = i\frac{{C_0}^2}{2\omega_\mathrm{q}}\left[\left(\frac{k_x}{\varepsilon_\perp}\right)^2\frac{\partial\varepsilon_\perp}{\partial\varepsilon_\mathrm{h}} + \left(\frac{q\pi}{h_\mathrm{p}\varepsilon_\parallel}\right)^2\frac{\partial\varepsilon_\parallel}{\partial\varepsilon_\mathrm{h}}\right]. \tag{29}$$

Here, $\frac{\partial\omega_\mathrm{q}}{\partial\varepsilon_\mathrm{h,r}}$ and $\frac{\partial\omega_\mathrm{q}}{\partial\varepsilon_\mathrm{h,i}}$ are the sensitivities of mode frequency with respect to the real and imaginary parts of the permittivity of the analyte. k_x, ω_q, and q are the tangential component of the wave vector, resonant frequency, and mode number, respectively.

The plasmonic mode confined the electric field at the n-Si NW and dielectric (analyte) interface, facilitated by the standing wave reflections at the HMM interface. The change in the permittivity of the analyte perturbs the resonance condition, as defined using eqn (28) and (29). Moreover, the perturbation of the complex anisotropic permittivity components of the HMM $\frac{\partial\varepsilon_\perp}{\partial\varepsilon_\mathrm{h}}$ and $\frac{\partial\varepsilon_\parallel}{\partial\varepsilon_\mathrm{h}}$ is defined using eqn (30)–(32) and illustrated in Fig. 6(a). The parallel permittivity $\varepsilon_\parallel$ is highly sensitive to the variation in ε_h.

$$\frac{\partial\varepsilon_\parallel}{\partial\varepsilon_\mathrm{h}} = \frac{q\varepsilon_\mathrm{m} + 2\varepsilon_\mathrm{h}}{q\varepsilon_\mathrm{h} + \varepsilon_\mathrm{m}} - mq\frac{q\varepsilon_\mathrm{m} + \varepsilon_\mathrm{h}}{(q\varepsilon_\mathrm{h} + \varepsilon_\mathrm{m})^2}, \tag{30}$$

$$\frac{\partial\varepsilon_\perp}{\partial\varepsilon_\mathrm{h}} = 1 - \mathrm{FF}, \tag{31}$$

$$q = \frac{1 + \mathrm{FF}}{1 - \mathrm{FF}}. \tag{32}$$

We investigated how changes in the real part of the analyte's permittivity perturb the resonant frequency within the first Brillouin zone, $k_\mathrm{max} \sim 2\pi/P$, as shown in Fig. 6(a) and (b). The sensitivity at the resonant frequency increased with the mode number because the gradient of the electric field at the NW interface was directly related to the mode number. Moreover, we studied the effect of the FF on the resonant frequency shifting following eqn (28), (29), (31) and (32), as illustrated in Fig. 6(b). As the FF decreased, the wavelength shifted closer to the natural plasma frequency of the NW. This made the perturbation of the anisotropic permittivity ($\varepsilon_\parallel$) stronger, leading to a larger frequency shift. Therefore, there was an increase in the resonant frequency shift as the FF decreased. Consequently, the LOD decreased as the electric field confinement was reduced, and less effective surface area was available to bind to NS1 molecules.

Furthermore, we investigated the effect of the NW's height on its sensitivity at the resonant wavelength of the 1st order, as depicted in Fig. 6(c). The sensitivity of the resonant frequency decreased as the NW's height increased, because the increase in the NW's height shifted the resonant wavelength further from the natural resonance, resulting in lower sensitivity.

3.6 Sensing performance

Reliable and efficient detection of target molecules requires target-specific biosensors. To detect the NS1 protein (produced by the dengue virus's RNA genome) with a higher LOD, we proposed a functionalized NW surface to bind with thiol-terminated single-stranded DNA (ssDNA) aptamers that have a high affinity for the target NS1 protein. However, the accumulation of plasma charge on the NW surface, as shown in Fig. S5 in the SI, hindered the binding of NS1-bound ssDNA to the functionalized NW. To hinder surface passivation, we proposed the use of thiol-terminated 6-mercaptohexanol (MCH) to effectively prevent non-selective binding of other proteins present in blood serum, as discussed in ref. 41. The detection of the NS1 protein is facilitated by the change in the local RI upon binding.

To investigate the binding event, we covered the outer cylindrical surface of the NW with a hollow cylinder having an inner radius of 'r' and a fixed outer radius of 40 nm. The bulk RI of this hollow cylinder was set equal to that of the NS1 protein (RI = 1.5) as discussed in Section 3 in the SI. Fig. 7(a) illustrates the physical estimation of the surface coverages by NS1 proteins in our n-Si NW biosensor structure. The reflection spectra of our structure at varying surface coverage of NS1 proteins are illustrated in Fig. 7(b). We observed that the resonance wavelength shift increases quadratically with surface occupation. The rate of change in resonance wavelength shift with respect to surface coverage was minimal at 0% coverage, increased with the

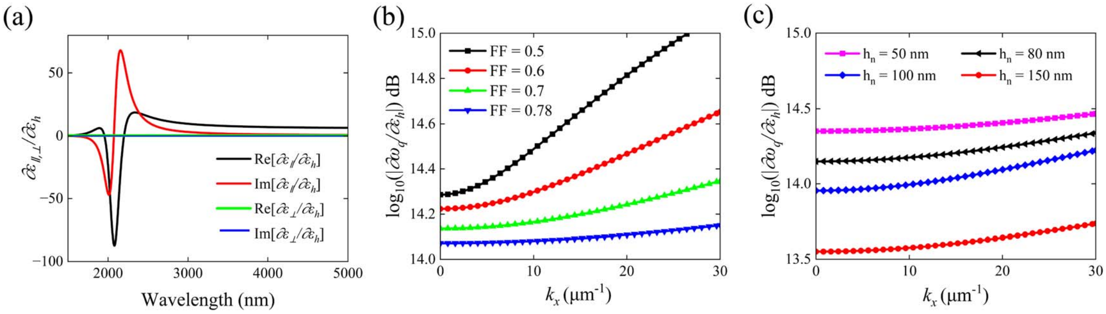

Fig. 6 (a) Illustration of the perturbation of $\varepsilon_\parallel$ and $\varepsilon_\perp$ over analyte permittivity ε_h. Red, black, green, and blue curves delineate the perturbation of the real and imaginary parts of $\varepsilon_\parallel$ and $\varepsilon_\perp$ over analyte permittivity. Perturbation of resonant frequency ω_q, indicating bulk sensitivity over change in ε_h at different (b) FFs and (c) heights of the n-Si NW under tangential wave vector k_x.

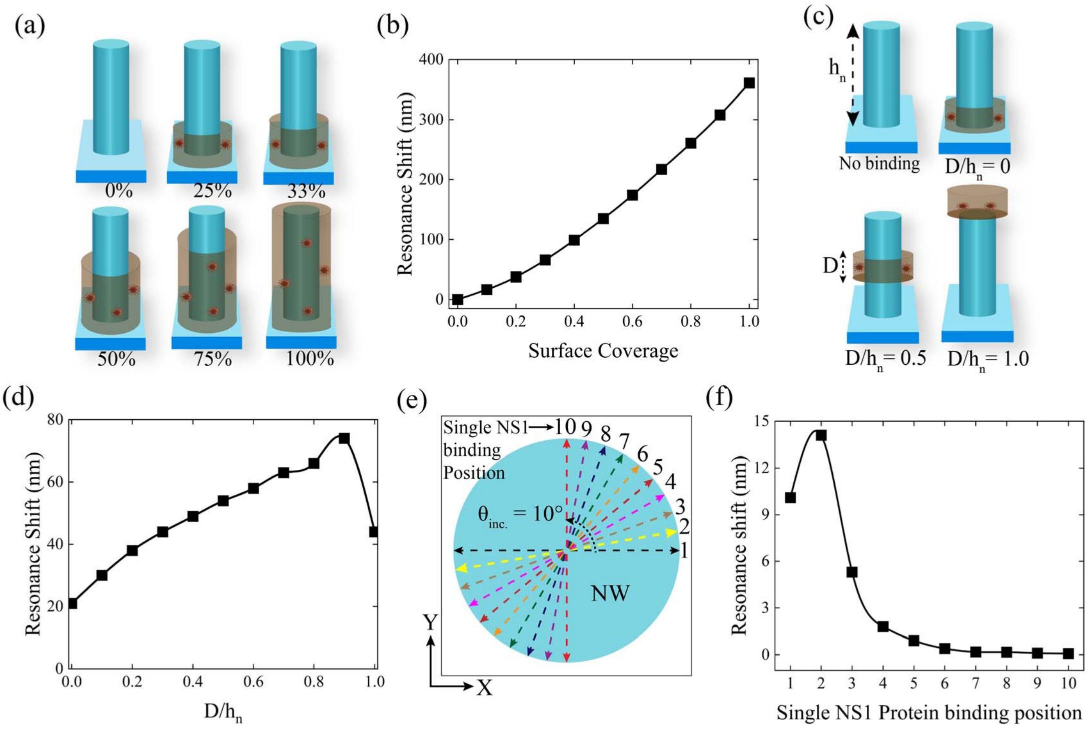

Fig. 7 (a) Representation of the schematic for numerical analysis of a unit cell with varying surface coverage of the NS1 protein, having h_n = 80 nm and (b) resulting resonance shift of reflection spectra. (c) Representation of the schematic for numerical analysis of a unit cell with varying D/h_n, where D is considered the height of the NS1 protein, which is 10% of the NW. (d) Resonance shifts of reflection spectra for different D/h_n. (e) Schematic illustration of the X–Y view of the NW indicating the position of binding a single NS1 protein with a dotted arrow and varying the position point θ_{inc} by 10°. (f) Resonance shift of reflection spectra for different positions of binding of a single NS1 protein, where maximum resonant shift was 14 nm in position 2.

percentage of coverage, and reached a maximum at 100% with 361 nm. This resonance wavelength shift came from the perturbations of electric field density due to changes in the local RI and an increase in electric field intensity above the out-of-plane surface. Due to the hyperbolic dispersion characteristic of our biosensor structure, changes in the local RI significantly altered k_z at the resonant wavelength, as described by eqn (26). Concurrently, the stronger electric field intensity above the planar surface (Fig. 3(d)) was more sensitive to local RI changes compared to the weaker field near the planar surface. Thus, we observed quadratic dependence of the resonance wavelength shift on surface occupation percentage.

A nanobiosensor should detect a single molecular binding event on the outer planar surface of the nanowire. The LOD of a nanobiosensor depends both on the rate of molecular flux diffusion toward the nanowire surface and its sensitivity to detect such events. We investigated the point detection capability of our structure by surrounding the NW surface with a cylindrical disk of 8 nm height at a point D, which corresponds to 10% of the NW's total height, as illustrated in Fig. 7(c). The resulting shifts in the resonance wavelength at various normalized positions D/h_n along the NW. We observed a maximum shift of 74 nm at $D/h_n = 0.9$, as shown in Fig. 7(d). On the other hand, there was a decrease to 44 nm at the NW's top surface ($D/h_n = 1$). We found that as the distance of the cylindrical disk from the planar surface increases, the resonance shift also increases initially. However, the ratio of the perturbed surface area to the change in the local RI remained almost constant. This enhancement of surface sensitivity above the planar surface is attributed to the stronger confinement of the electric field near the NW, as illustrated in Fig. 3(d). The effect of the localized electric field is further confirmed by the immediate decrease in resonance shift as D/h_n approaches 1. This simulated molecular binding at the top surface of the NW, where the field primarily existed as an evanescent field. Furthermore, we studied the point detection capability of our biosensor structure by introducing a single molecule at the sensor surface parallel to the NW, as shown in Fig. 7(e). A single NS1 protein, with an average volume of ~90 nm^3, was positioned on the x-axis and subsequently rotated in an anticlockwise direction by $\theta_{inc} = 10°$ from the x-axis to the y-axis direction. The resulting shift in resonant frequency, as demonstrated in Fig. 7(f), confirms the ultrasensitive response of our sensor structure. A resonant shift of ~10 nm was observed for a single NS1 protein bound at the top surface of the NW at position-0. Moreover, the resonance frequency shift reached its maximum value of 14 nm when the NS1 protein was bound at an angle of 10° (position-1) from the horizontal axis. This enhanced sensitivity was attributed to the maximum electric field intensity and charge density at this specific angle, as illustrated in Fig. 3(c). Beyond 10°, the resonance frequency shift declined, reaching its lowest shift of ~0.08 nm at 90° (position-10), where the electric field intensity was minimal. This non-uniform confinement of the electric field around the

NW surface at the nanoscale leads to nonlinear sensitivity across the surface. Additionally, our proposed biosensor structure can detect a maximum resonant shift of 14 nm for a single NS1 protein, which is well above the detection limit of typical measurement units, accounting for noise. The corresponding mass sensitivity of our biosensor structure was calculated to be 0.192 nm kDa^{-1}, as discussed in Section 8 in the SI.

3.7 Diffusion analysis of molecules

The effective permittivity of the heterogeneous mixture of NS1 protein and water at different molar concentrations was determined using eqn (15). We observed a linear shift in the resonance wavelength as we increased X from 0 to 100%, as depicted in Fig. 8(a) and (b). Moreover, we analyzed the response behavior of our biosensor structure for detecting other biomolecules such as hemoglobin and glucose, which are given in Section 9 in the SI. The resonant wavelength shift induced by one NS1 molecule ($\Delta\lambda$) must exceed the root-sum-square of all readout noise contributions within the measurement bandwidth. This can be quantified through the noise-equivalent wavelength shift, which was ~1 nm.[46] Therefore, we considered a minimum measurable resonance shift of 1 nm and obtained a reliable detection of the NS1 concentration above 0.267%. However, the resulting LOD lies below the clinical detection threshold. Notably, a significant enhancement in the LOD can be achieved by functionalizing the NW with ssDNA aptamers that selectively bind the NS1 protein. These ssDNA molecules diffuse through the solution and attach to the NW surface. The diffusion and binding eqn (16)–(18) describe the distribution of the NS1 protein concentration. The numerical solutions to these equations for our proposed biosensor structure geometry are depicted in Fig. 8(c). The concentration of ssDNA molecules gradually decreased towards the surface of our biosensor structure, indicating a molecular flux directed normal to the surface. The concentrated ssDNA molecules were transported to the surface and predominantly bound to the NW surface normal to the x- and y-directions. In these regions, the local concentration was lower, resulting in a continuous diffusion flux into these regions. The ssDNA molecules diffused and bound to the functionalized n-Si NW surface. The number of molecules captured by the sensor surface at nanomolar (nM), picomolar (pM), and femtomolar (fM) concentrations of the NS1 solution is illustrated in Fig. 8(d). We observed that the number of biomolecules captured at the sensor surface increased over time, regardless of the concentration of NS1 solution, as molecules from further distances were able to diffuse to the sensor surface. However, the rate at which the molecules bound to the sensor surface was significantly higher at higher analyte concentrations compared to lower concentrations. The weaker diffusion force in the low analyte concentration limits the capability of detecting a single molecule binding event on the sensor surface. Moreover, the solution maintained a linear relationship on a logarithmic scale for captured molecules and time intervals. Hence, a slight change in the required time interval to capture a single molecule at the fM concentration was much larger than that for the pM concentration in the linear time domain. This time interval restricted the LOD. Fig. 8(e) illustrates the required time intervals for a single NS1 molecule to bind to the surface of our biosensor structure at various concentrations of the NS1 solution. The binding times were reliable, measuring approximately 17 μs and 148 s for 1 nM & 1 pM concentrations,

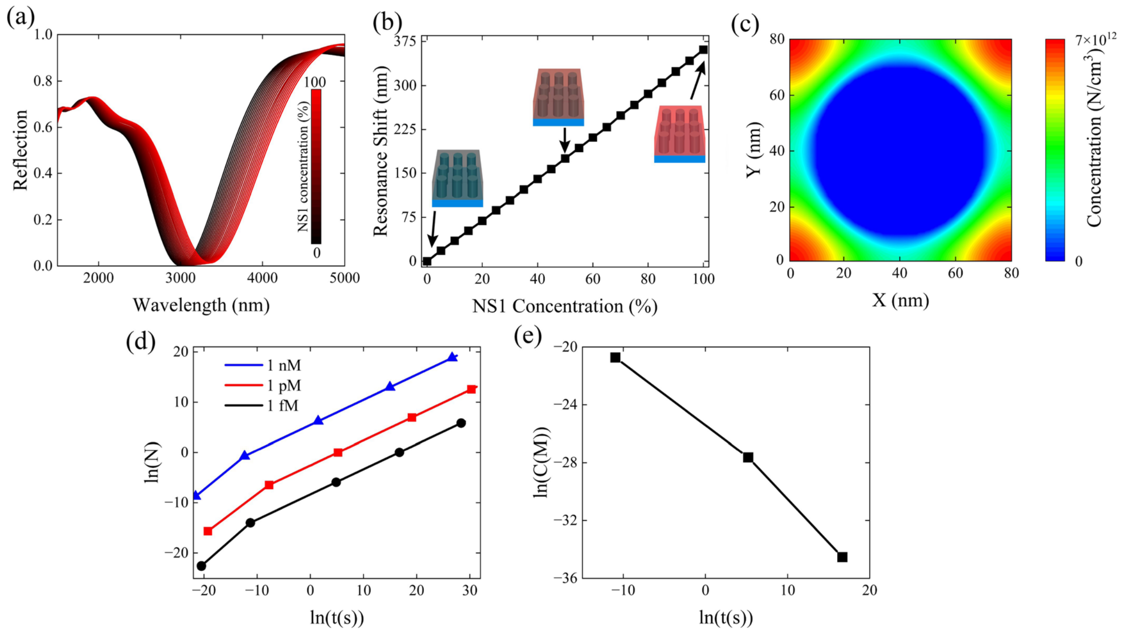

Fig. 8 The corresponding bulk response of (a) reflection spectra and (b) resonant frequency shift at different concentrations of NS1 protein solution using EMT. The insets present the increasing concentration of NS1. (c) Illustration of the local concentration of the NS1 protein at an instant around the n-Si NW. (d) Depiction of the total number of captured molecules (N) for different molar concentrations (nM, pM, and fM) of NS1 protein solution at a given time (t) on the NW surface on a logarithmic scale. (e) The required time to capture a single NS1 protein molecule of different initial molar concentrations (C(M)) of the solution of the proposed HMM biosensor structure on a logarithmic scale.

Table 1 Comparative performance analysis between different previous studies

Structure	Wavelength (μm)	Sensitivity	LOD	Reference
Gold triangular nanoparticles	0.5–0.7	<7.33 nm mM^{-1}	0.3 mM	E. Chowdhury[42]
Au/1D photonic crystal	0.6–0.8	53.5 nm per RIU	0.009 g dl^{-1}	M. Shaban[43]
DNA-modified plasmonic sensor	0.75–0.9	—	1.1 mg ml^{-1}	A. Guardado[41]
PAMAM-based optical sensor	2.5–10	—	1 pM	N. Omar[44]
Ag/Si multilayered HMM	0.8–2	3450 nm per RIU	—	M. Baqir[45]
TiN nanowire HMM sensor	1–3	11 nm per bacterium	0.00008 RIU	D. Sarker[25]
Si-nanowire HMM sensor	1.5–5	14 nm per NS1 molecule	0.691 pM	This work

respectively. However, it required approximately 199 days to detect a single molecule at a 1 fM concentration. Moreover, to perform rapid detection & monitoring, a label-free real-time biosensor requires instantaneous detection. Abraham *et al.* allowed the NS1 protein molecule to thermally diffuse and bind the functionalized nanowire surface and continued the experiment for 3–8 minutes to obtain a saturated signal of LSPR shifting to detect the DENV2 NS1 protein.[41] In this study, we assumed a maximum idle time of 5 minutes for the sensor before it reaches saturation. Thus, we measured the LOD of our proposed biosensor structure to be approximately 0.691 pM, demonstrating its high sensitivity for biomolecular detection.

4 Comparative analysis

We conducted a comparative analysis of performance parameters between our proposed structures and previously reported sensors, as listed in Table 1. We performed a comparative analysis of sensor sensitivity and the limit of detection (LOD) in relation to other studies. Chowdhury *et al.* proposed a triangular nanoparticle sensor, whose sensitivity is low and the LOD is large.[42] Hence, this kind of structure is not conducive to detecting tiny molecules. However, 1D photonic crystal structures and plasmonic sensors increase sensitivity compared to nanoparticle-based structures; however, the sensitivity and LOD of these sensors were not sufficient for miniature molecules.[41,43] On the other hand, PAMAM-based optical sensors can exhibit a high LOD, which can be conducive to tiny molecules such as the dengue NS1 protein.[44] In addition, the HMM sensor is an excellent option for addressing these issues. Baqir *et al.* proposed a multilayered HMM structure with excellent sensitivity. Furthermore, Sarker *et al.* proposed a nanowire-based HMM structure, which reached excellent sensitivity and FOM for miniature microbes.[25] However, these HMM structures were constructed using materials that were not readily available; in contrast, we developed a nanowire HMM sensor structure made of silicon, which was not previously studied. Moreover, we achieved an excellent sensitivity of 14 nm per dengue NS1 protein with an outstanding LOD of 0.691 pM in our proposed structure. Hence, we can infer that our proposed structure will efficiently detect nanoscale samples.

5 Conclusion

We proposed an n-Si NW-based HMM biosensor structure and analyzed its optical characteristics using the FDTD method and TMM. We employed the EMT to analyze the hyperbolic behaviour of the biosensor structure. We obtained the hyperbolic region of the n-Si NW after a wavelength of 2200 nm. We optimized the impedance matching of the structure and observed a perfect reflection notch at 2999 nm. Moreover, our proposed structure exhibited angle insensitivity due to its extreme hyperbolic characteristic. To successfully detect the dengue virus, we injected the NS1 protein by changing the surrounding local RI of the n-Si NW and calculated the shift in the resonance wavelength of our proposed sensor structure. We further demonstrate enhanced electric field confinement that enabled the detection of a single NS1 protein. After detecting a single NS1 protein, we evaluated its mass sensitivity which is 0.192 nm kDa^{-1}. After that, we analyzed the diffusion rate of the NS1 protein into the n-Si NW biosensor structure by employing diffusion equations to obtain the relationship between the required time and the number of NS1 molecules captured for different molar concentrations of NS1 protein solution. Our proposed sensor structure demonstrated an LOD of 0.691 pM, which means that it can detect viruses of lower concentrations. Our research paves the way for the design and fabrication of Si-based sensors for label-free detection.

Author contributions

B. Golder and Z. Salman conducted the investigation and analysis, wrote the manuscript, and prepared the figures and SI. Both authors contributed equally to this work. R. Das conducted the investigation and analysis and wrote the manuscript. A. Ahammad provided assistance and supervision throughout the study. All the authors reviewed and approved the manuscript.

Conflicts of interest

The authors declare no conflict of interest.

Data availability

The data supporting the findings detailed in the article are not readily accessible. However, interested individuals can obtain it by making a reasonable request to the authors.

Supplementary information: fabrication methods, material properties, additional theoretical derivations, and other supporting performance graphs of this work. See DOI: **https://doi.org/10.1039/d5na00714c**.

Acknowledgements

The authors express their heartfelt appreciation to the Department of Electrical and Electronic Engineering (EEE) at the Shahjalal University of Science and Technology (SUST) for providing the necessary resources to complete the work.

Notes and references

1 J. N. Anker, W. P. Hall, O. Lyandres, N. C. Shah, J. Zhao and R. P. Van Duyne, *Nat. Mater.*, 2008, **7**, 442–453.
2 R. Das, B. Golder, D. Sarker and A. Ahammad, *Opt. Mater. Express*, 2024, **14**, 1909–1923.
3 A. Taharat, M. A. Kabir, A. I. Keats, A. Rakib and R. H. Sagor, *Opt. Commun.*, 2025, **578**, 131495.
4 J. Xu, H. Yao, T. Chi, H. Cheng, W. Yue, B. Liu, X. Zhang, S. Li, B. Zhang, Y. Lu, *et al.*, *Appl. Opt.*, 2024, **63**, 4125–4130.
5 C. Hong, I. Hong, Y. Jiang and J. C. Ndukaife, *Adv. Opt. Mater.*, 2024, **12**, 2302603.
6 T. Takahashi, T. Hizawa, N. Misawa, M. Taki, K. Sawada and K. Takahashi, *J. Micromech. Microeng.*, 2018, **28**, 054002.
7 J. Qin, S. Jiang, Z. Wang, X. Cheng, B. Li, Y. Shi, D. P. Tsai, A. Q. Liu, W. Huang and W. Zhu, *ACS Nano*, 2022, **16**, 11598–11618.
8 M. Svedendahl, S. Chen, A. Dmitriev and M. Kall, *Nano Lett.*, 2009, **9**, 4428–4433.
9 P. N. Prasad, *Introduction to Biophotonics*, John Wiley & Sons, 2004.
10 M. M. Hassan, F. S. Sium, F. Islam and S. M. Choudhury, *Sens. Biosens. Res.*, 2021, **33**, 100429.
11 P. Wang, M. E. Nasir, A. V. Krasavin, W. Dickson, Y. Jiang and A. V. Zayats, *Acc. Chem. Res.*, 2019, **52**, 3018–3028.
12 M. Kheirollahpour, N. Shokoufi and M. Lotfi, *Crit. Rev. Anal. Chem.*, 2025, 1–29.
13 V. S. Chaudhary, D. Kumar and S. Kumar, *IEEE Sens. J.*, 2021, **21**, 17800–17807.
14 M. R. Hasan, P. Sharma, S. Khan, U. M. Naikoo, K. Bhalla, M. Abdin, N. Malhotra, T. M. Aminabhavi, N. P. Shetti and J. Narang, *Sens. Diagn.*, 2025, **4**, 7–23.
15 Y. Ma, Y. Leng, D. Huo, D. Zhao, J. Zheng, P. Zhao, H. Yang, F. Li and C. Hou, *Food Chem.*, 2023, **429**, 136850.
16 L. Ferrari, J. S. T. Smalley, Y. Fainman and Z. Liu, *Nanoscale*, 2017, **9**, 9034–9048.
17 N. A. Salama, M. Desouky, S. Obayya and M. A. Swillam, *Sci. Rep.*, 2020, **10**, 11529.
18 D. Lu, J. J. Kan, E. E. Fullerton and Z. Liu, *Nat. Nanotechnol.*, 2014, **9**, 48–53.
19 M. Mahmoodi, S. H. Tavassoli, O. Takayama, J. Sukham, R. Malureanu and A. V. Lavrinenko, *Laser Photonics Rev.*, 2019, **13**, 1800253.
20 H.-Z. Gao, W.-R. Xu, M.-C. Li, N. Ilyas, J.-M. Wang, W. Li and X.-D. Jiang, *Opt Laser. Technol.*, 2022, **151**, 108034.
21 K. V. Sreekanth, Y. Alapan, M. ElKabbash, E. Ilker, M. Hinczewski, U. A. Gurkan, A. De Luca and G. Strangi, *Nat. Mater.*, 2016, **15**, 621–627.
22 N. Vasilantonakis, G. A. Wurtz, V. A. Podolskiy and A. V. Zayats, *Opt. Express*, 2015, **23**, 14329–14343.
23 R. Yan, T. Wang, X. Yue, H. Wang, Y.-H. Zhang, P. Xu, L. Wang, Y. Wang and J. Zhang, *Photonics Res.*, 2021, **10**, 84–95.
24 G. V. Naik, V. M. Shalaev and A. Boltasseva, *Adv. Mater.*, 2013, **25**, 3264–3294.
25 D. Sarker and A. Zubair, *Phys. Chem. Chem. Phys.*, 2024, **26**, 10273–10283.
26 Y. Gao, S. Zhang, T. Aili, J. Yang, Z. Jia, J. Wang, H. Li, L. Bai, X. Lv and X. Huang, *Biosens. Bioelectron.*, 2022, **204**, 114035.
27 J. D. Joy, M. S. Rahman, R. Rahad and M. H. Chowdhury, *Measurement*, 2025, **242**, 116049.
28 M. O. Faruque, R. Al Mahmud and R. H. Sagor, *Plasmonics*, 2022, **17**, 203–211.
29 S. H. Shakib, N. H. Niloy and A. Ahammad, *Heliyon*, 2025, **11**(5), e43072.
30 H. A. Macleod and H. A. Macleod, *Thin-film Optical Filters*, CRC press, 2010.
31 Z. Salman, R. Das, B. Golder and A. Ahammad, *International Conference on Innovations in Science, Engineering and Technology (ICISET)*, 2024, pp. 1–6.
32 A. Poddubny, I. Iorsh, P. Belov and Y. Kivshar, *Nat. Photonics*, 2013, **7**, 948–957.
33 C. H. Taubes, *Modeling Differential Equations in Biology*, Cambridge University Press, 2008.
34 Y. Liu, Q. Guo, S. Wang and W. Hu, *Appl. Phys. Lett.*, 2012, **100**(15), 153502.
35 S. L. Chuang, *Physics of Photonic Devices*, John Wiley & Sons, 2012.
36 K.-T. Lee, S. Seo, J. Y. Lee and L. J. Guo, *Adv. Mater.*, 2014, **26**(36), 6324–6328.
37 V. R. Shrestha, S.-S. Lee, E.-S. Kim and D.-Y. Choi, *Sci. Rep.*, 2014, **4**, 4921.
38 X. Yue, T. Wang, Y. Cai, R. Yan, L. Wang, H. Wang, E. Lv, X. Yuan, J. Zeng, X. Shu, et al., *Photonics Res.*, 2024, **13**, 113–124.
39 Y.-K. R. Wu, A. E. Hollowell, C. Zhang and L. J. Guo, *Sci. Rep.*, 2013, **3**, 1194.
40 M. H. Weik, *Computer Science and Communications Dictionary*, Springer, 2000, pp. 986.
41 A. Vázquez-Guardado, F. Mehta, B. Jimenez, A. Biswas, K. Ray, A. Baksh, S. Lee, N. Saraf, S. Seal and D. Chanda, *Nano Lett.*, 2021, **21**, 7505–7511.
42 E. Chowdhury and A. Zubair, *Opt. Mater. Express*, 2022, **12**, 2212–2225.
43 M. Shaban, A. M. Ahmed, E. Abdel-Rahman and H. Hamdy, *Sci. Rep.*, 2017, **7**, 41983.
44 N. A. S. Omar, Y. W. Fen, I. Ramli, A. R. Sadrolhosseini, J. Abdullah, N. A. Yusof, Y. M. Kamil and M. A. Mahdi, *Polymers*, 2021, **13**, 762.
45 M. Baqir, A. Farmani, T. Fatima, M. Raza, S. Shaukat and A. Mir, *Appl. Opt.*, 2018, **57**, 9447–9454.
46 G. Palermo, G. E. Lio, M. Esposito, L. Ricciardi, M. Manoccio, V. Tasco, A. Passaseo, A. De Luca and G. Strangi, *ACS Appl. Mater. Interfaces*, 2020, **12**, 30181–30188.